REVIEW

Check for updates

Journal of
Sensor Science and Technology

The Korean Sensors Society

Light-Activated Gas Sensors for Next-Generation Sensing Platforms: Materials Engineering, System-Level Integration, and AI-Assisted Analysis

Yun-Haeng Cho[1] and **Jun Min Suh**[1,2,+]

[1]*Department of Materials Science and Engineering, Research Institute of Advanced Materials, Seoul National University, Seoul 08826, Republic of Korea*
[2]*School of Transdisciplinary Innovations, Seoul National University, Seoul 08826, Republic of Korea*

Cite This: *J. Sens. Sci. Technol. Vol. 35, No. 4 (2026) 352-365*

https://doi.org/10.46670/JSST.2026.35.4.352

ABSTRACT: Light-activated gas sensors have attracted considerable attention as a promising room-temperature alternative to conventional thermally activated chemiresistive sensors for low-power, miniaturized sensing platforms. However, their practical implementation remains challenging because of inefficient light utilization, UV-dependent photoactivation, cross-sensitive responses, and signal variations under real-world environmental conditions. This review summarizes recent advances in light-activated gas sensors from the perspectives of materials engineering, system-level integration, and AI-assisted analysis. Materials engineering strategies, including three-dimensional nanostructure design, functional overlayers, and photosensitizer engineering, are discussed for improving light utilization, selective gas transport, and visible-light activation. Ambient-light-driven and micro-light-emitting diode-integrated sensing platforms are further introduced for low-power, real-time monitoring with wireless signal readout. In addition, AI-assisted approaches based on time-varying light modulation and environmental compensation are discussed for selective gas recognition under practical operating conditions. Collectively, these advances highlight the importance of integrating materials, device engineering, and analytical strategies to develop reliable and low-power light-activated gas-sensing platforms for environmental monitoring, wearable electronics, and mobile sensing applications.

KEYWORDS: *Light-activated gas sensors, Nanostructures, Materials engineering, Micro-light-emitting diodes, Artificial intelligence*

1. INTRODUCTION

As connected sensing technologies become increasingly integrated into everyday environments, advanced gas-sensing technologies have emerged as key components of next-generation monitoring platforms [1-5]. In particular, real-time gas monitoring of chemical information is crucial for a broad range of practical applications, including industrial safety [6], air-quality monitoring [7], food-freshness assessment [8], odor analysis [9], and noninvasive health monitoring through breath analysis [10]. To meet these demands, various gas-sensing technologies, including capacitive [11], optical [12], cantilever-based [13], thermometric [14], field-effect transistor [15], solid-state electrochemical [16], surface acoustic wave [17], and chemiresistive sensors [18], have been investigated. Among these technologies, chemiresistive gas sensors are particularly attractive for IoE applications owing to their simple architecture, ease of fabrication, cost-effectiveness, compatibility with integrated electronics, and high sensitivity toward diverse gaseous analytes [19,20].

Despite these advantages, conventional chemiresistive gas sensors still suffer from a major limitation because of their reliance on elevated operating temperatures (typically 200–400°C) to activate surface oxygen species and facilitate redox reactions with target gas molecules [21-23]. Although thermal activation offers high sensitivity and rapid reaction kinetics, it requires continuous power consumption and imposes thermal stress on adjacent electronic components and temperature-sensitive interfaces. Consequently, these limitations hinder the miniaturization and integration of conventional gas sensors

[+]Corresponding author: junminsuh@snu.ac.kr
Received : Jun. 24, 2026, Revised : Jul. 3, 2026, Accepted : Jul. 6, 2026

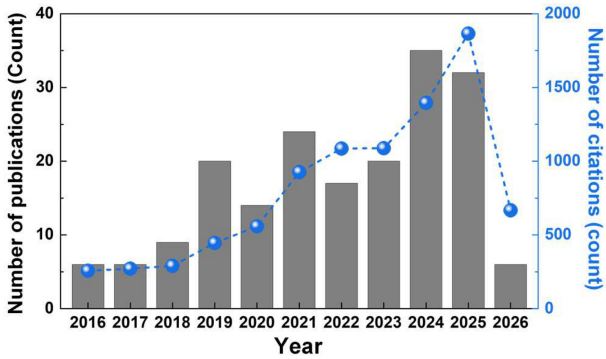

Fig. 1. Annual publication and citation trends for light-activated gas sensors from 2016 to 2026, based on a Web of Science database searched on May 29, 2026 using the keyword "light-activated gas sensor" and "photoactivated gas sensor."

into battery-powered electronics, wearable devices, and biologically interfaced sensing systems [24,25].

To overcome these issues, light activation has been widely investigated as a room-temperature alternative for chemiresistive gas sensors [26-31]. Under light illumination, photogenerated charge carriers can promote surface reactions involving adsorbed oxygen species and target gas molecules, enabling gas sensing without external heating [32,33]. In particular, light-emitting diodes provide compact and low-power excitation sources that can be readily integrated into miniaturized sensing platforms. The overall increase in publications and citations related to light-activated gas sensors also reflects the growing interest in this approach for next-generation sensing platforms (Fig. 1). However, the gas-sensing performance of light-activated gas sensors often remains limited by inefficient light utilization, photocarrier recombination, and insufficient gas accessibility. In addition, the wide bandgaps of many metal oxide semiconductors restrict photoactivation to UV illumination, limiting compatibility with ambient and indoor light sources [34]. Cross-sensitive responses and humidity-induced signal variations further reduce sensing reliability under practical conditions [35]. Collectively, these challenges underscore the need for material, light-source, device-platform, and signal-analysis strategies that can improve sensing performance and reliability under realistic operating environments.

This review comprehensively summarizes recent advances in light-activated gas sensors from the perspectives of materials engineering, system-level integration, and AI-assisted analysis. Materials engineering strategies, including nanostructure engineering for enhanced light utilization and gas accessibility, functional overlayers for selective gas transport, and photosensitizer engineering for visible-light activation, are discussed. Ambient-light-driven and micro-light-emitting diode (μLED)-integrated sensing platforms combined with wireless electronics and mobile interfaces are also introduced for low-power real-time monitoring. In addition, AI-assisted analysis based on time-varying light modulation and environmental compensation is discussed for selective gas recognition under practical conditions. Overall, this review provides a comprehensive perspective on material, device, and analytical strategies for developing high-performance, low-power, and reliable light-activated gas-sensing platforms suitable for practical applications.

2. MATERIALS ENGINEERING FOR HIGH-PERFORMANCE GAS SENSORS

Materials engineering has emerged as a key strategy for enhancing the performance of light-activated gas sensors [36-39]. Their sensing performance depends not only on the intrinsic electronic properties of the sensing material but also on efficient light utilization and the accessibility of target gas molecules to the active surface. Accordingly, strategies such as nanostructure engineering, functional overlayers, surface modification, and dopant engineering have been extensively explored to optimize light absorption, charge-carrier separation, gas transport, and surface reaction kinetics.

2.1 Nanostructure Engineering for Enhanced Light Utilization and Gas Accessibility

Nanostructure engineering is widely used to improve the gas sensing performance by controlling the geometry of the sensing layer. In particular, three-dimensional (3D) nanostructures can enhance the interaction between incident light and the sensing material through multiple scattering, internal reflection, and light confinement (Fig. 2) [40]. Their porous frameworks further facilitate gas diffusion throughout the sensing layer. Therefore, these structural features directly affect light utilization, gas transport, and electrical response.

Cho et al. systematically designed highly periodic 3D thin-shell TiO_2 nanostructures (denoted as 3D TiO_2) for high-performance NO_2 sensing under light illumination. The 3D TiO_2 nanonetwork provides a large surface area and interconnected porous pathways, allowing gas molecules to access both the exterior and interior surfaces of the sensing layer (Fig. 2(a)). Furthermore, the narrow necks between adjacent TiO_2 shells act as sensitive conduction channels, where the resistance can be effectively modulated by gas adsorption.

To optimize the structural design of the 3D TiO_2 nanonetwork, the authors systematically investigated the effects of both the total film thickness and TiO_2 shell thickness

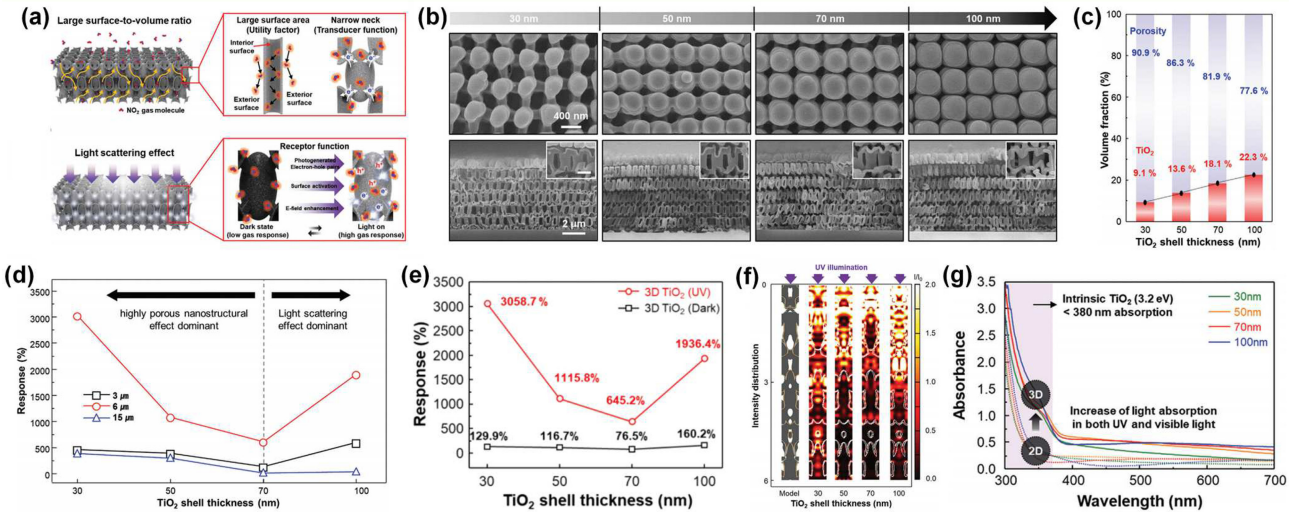

Fig. 2. Geometric advantages for light-activated NO_2 gas sensing. (a) Schematic illustration of enhanced NO_2 diffusion and light scattering in highly periodic 3D TiO_2 nanonetworks. (b) Top-view and cross-sectional scanning electron microscope (SEM) images of 3D TiO_2 with TiO_2 thin-shell thicknesses of 30, 50, 70, and 100 nm. (c) Air and TiO_2 volume fractions as a function of shell thickness. (d) Calculated responses of 3D TiO_2 to 5 ppm NO_2 under UV illumination with different TiO_2 thin-shell and film thicknesses. (e) Responses of 3D TiO_2 as a function of shell thickness under dark and UV illumination. (f) Simulated E-field intensity distributions of 3D TiO_2 under UV illumination as a function of TiO_2 thin-shell thickness. (g) UV–vis absorbance spectra of 3D TiO_2 and planar TiO_2 thin films with different thin-shell thicknesses. Absorbance was calculated from the measured total transmittance. Adapted from Ref. [40].

on NO_2 sensing performance. Among the investigated structures, the 6 μm-thick 3D TiO_2 exhibited the highest NO_2 response, indicating that an optimized film thickness is essential for balancing light utilization and gas diffusion (Fig. 2(d)). In the 3 μm-thick structure, light scattering within the sensing layer was limited, whereas the 15 μm-thick structure reduced effective light penetration and gas diffusion, resulting in a lower overall sensing response. As the shell thickness increased from 30 to 100 nm, the air volume fraction decreased from 90.9% to 77.6%, leading to reduced pore volume and gas accessibility (Fig. 2(b,c)). Among the tested structures, the 6 μm-thick 3D TiO_2 with a 30 nm thin shell exhibited the highest response to 5 ppm NO_2 under UV illumination (Fig. 2(d)). The sensing response gradually decreased as the shell thickness increased from 30 to 70 nm because reduced porosity restricted gas accessibility. Interestingly, the response increased at a shell thickness of 100 nm, suggesting that enhanced light scattering within the thicker TiO_2 shell partially compensated for the reduced gas accessibility. These results highlight that the sensing performance of 3D TiO_2 is determined by the balance between gas accessibility and light utilization.

The role of light activation was further elucidated by comparing the NO_2 responses under dark and UV illumination conditions (Fig. 2(e)). Under dark conditions, all structures exhibited relatively low responses regardless of the shell thickness. By contrast, UV illumination significantly enhanced the overall response, and the 30 nm thin-shell structure achieved the highest response of 3058.7% to 5 ppm NO_2. This enhanced performance is attributed to UV-induced photoactivation, which facilitates electron–hole pair generation and surface reactions with NO_2 molecules. The optical advantage of the 3D structure was further supported by E-field simulation and UV–vis absorbance analysis (Fig. 2(f,g)). The calculated E-field distributions confirmed effective light confinement within the 3D TiO_2 network, while the UV–vis spectra showed higher absorbance of 3D TiO_2 than planar TiO_2 in both UV and visible-light regions. Collectively, these findings highlight the critical role of nanostructure engineering in simultaneously optimizing light utilization and gas accessibility, two key factors governing the performance of light-activated gas sensors.

2.2 Functional Overlayers for Selective Gas Transport

Selectivity is one of the key requirements for the practical deployment of light-activated gas sensors, because real-world environments contain multiple interfering gases that induce cross-sensitive responses [35,41]. However, conventional chemiresistive sensors still struggle to distinguish target gases with similar adsorption behavior or overlapping reaction characteristics.

To address this issue, Lee et al. developed ZIF-8-functionalized 3D ZnO nanostructures for selective NO_2

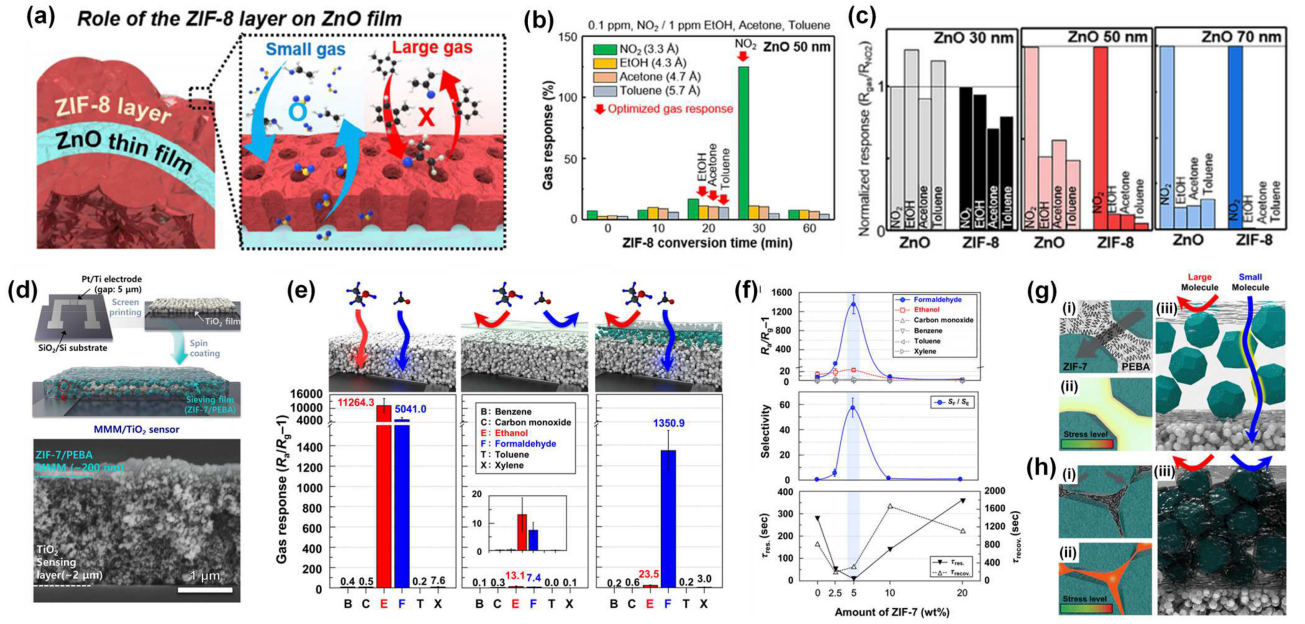

Fig. 3. Functional overlayers for selective gas transport and molecular discrimination. (a) Schematic illustration of size-selective gas transport through a ZIF-8 overlayer on ZnO thin films. (b) Gas responses of ZnO/ZIF-8 sensors to 0.1 ppm NO_2 and 1 ppm interfering gases as a function of ZIF-8 conversion time. (c) Normalized responses of ZnO and ZnO/ZIF-8 sensors with different ZnO thicknesses. Adapted from Ref. [42]. (d) Fabrication process and cross-sectional SEM image of the ZIF-7/PEBA MMM-coated TiO_2 sensor. (e) Gas responses of bare TiO_2, pure PEBA/TiO_2, and 5MMM/TiO_2 sensors under UV illumination. (f) Effects of ZIF-7 loading on gas response, selectivity, and response/recovery times of MMM/TiO_2 sensors. (g,h) Schematic illustrations of gas penetration, stress distribution, and polymer configuration in ZIF-7/PEBA MMMs with mild and excessive ZIF-7 loading, respectively. Adapted from Ref. [43].

sensing under light activation [42]. The ZIF-8 overlayer features well-defined micropores that allow relatively small NO_2 molecules to reach the ZnO surface while restricting the diffusion of larger interfering gases, including ethanol, acetone, and toluene (Fig. 3(a)). This pore-size-dependent transport promotes preferential NO_2 access to the photoactivated ZnO surface and reduces cross-sensitive responses. The ZIF-8 conversion time was systematically varied from 0 to 60 min to optimize molecular sieving (Fig. 3(b)). Insufficient ZIF-8 formation failed to effectively block interfering molecules, whereas excessive conversion limited NO_2 diffusion toward the ZnO surface. As a result, the highest NO_2 selectivity was achieved at a conversion time of 30 min. Beyond molecular sieving, the ZIF-8 overlayer also enhanced the NO_2 response through interfacial photoactivation at the ZIF-8/ZnO interface. The sensing performance was further optimized by varying the ZnO thickness from 30 to 70 nm, and the ZIF-8-functionalized 70 nm ZnO sensor showed high selectivity toward NO_2 with negligible responses to interfering gases (Fig. 3(c)). These results demonstrate that ZIF-8 functionalization can improve selectivity by controlling molecular transport to the photoactivated ZnO surface.

In a related approach, Jo et al. employed a ZIF-7/PEBA mixed-matrix membrane (MMM) on mesoporous TiO_2 sensing layer to improve HCHO selectivity through controlled gas transport (Fig. 3(d)) [43]. The mesoporous TiO_2 film served as the photoactivated sensing layer, while the ZIF-7/PEBA membrane regulated molecular transport before gas molecules reached the TiO_2 surface. Bare TiO_2 showed strong responses to both HCHO and ethanol, indicating limited discrimination between these gases (Fig. 3(e)). In contrast, pure PEBA/TiO_2 largely suppressed the gas responses because the polymer layer hindered gas diffusion for all gases toward the sensing layer. After incorporating ZIF-7 into the PEBA matrix, the MMM-coated TiO_2 sensor maintained a strong HCHO response while reducing the ethanol response, indicating the formation of selective pathways for HCHO transport. The ZIF-7 loading was a key parameter for balancing molecular sieving and gas permeability (Fig. 3(f)). The optimized membrane exhibited high HCHO selectivity and rapid response–recovery characteristics, whereas excessive ZIF-7 loading reduced the sensing performance. This behavior is attributed to changes in gas transport pathways and polymer-chain configuration within the mixed-matrix membrane. At an appropriate ZIF-7 loading, the membrane provides effective diffusion pathways for HCHO while maintaining sufficient gas permeability (Fig. 3(g)). However, excessive ZIF-7 loading increases local stress and restricts polymer chain mobility,

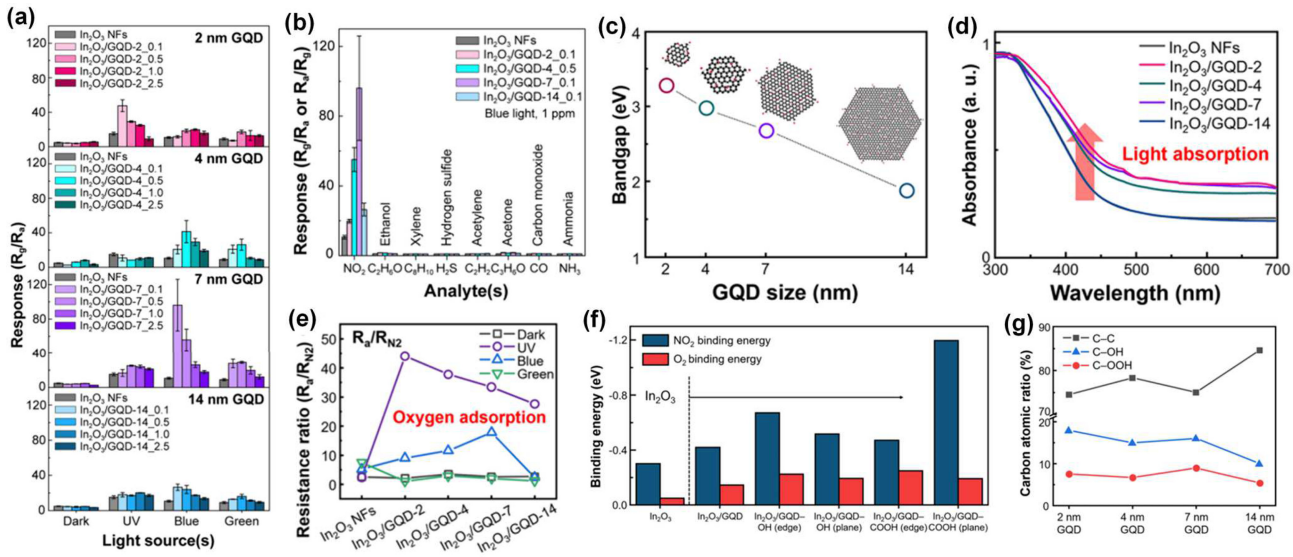

Fig. 4. Bandgap engineering of GQD photosensitizers for tunable light-spectrum-activated NO_2 sensing. (a) NO_2 responses of In_2O_3/GQD sensors with different GQD sizes and loadings under dark, UV, blue, and green illumination. (b) Gas selectivity of In_2O_3/GQD sensors under blue-light illumination. (c) Size-dependent optical bandgaps of GQDs. (d) UV–vis absorbance spectra of pristine In_2O_3 nanofibers and GQD-decorated In_2O_3 nanofibers. (e) Baseline resistance ratios in air and N_2 atmospheres under different light sources. (f) DFT-calculated binding energies of NO_2 and O_2 on pristine and GQD-functionalized In_2O_3 surfaces. (g) Atomic ratios of C–C, C–OH, and C–COOH groups in GQDs with different sizes. Adapted from Ref. [38].

thereby limiting gas transport through the membrane (Fig. 3(h)). Collectively, these findings highlight that functional overlayer engineering provides an effective strategy for enhancing molecular discrimination through rational control of pore structure, membrane composition, and filler loading.

2.3 Bandgap Engineering for Visible-Light Activation

Light-activated metal oxide gas sensors based on TiO_2, ZnO, SnO_2, and In_2O_3 traditionally relied on UV illumination because of their wide intrinsic bandgaps, which limit photoactivation to the UV or near-UV region [44–46]. From a practical perspective, visible-light activation is more suitable for sensing platforms because indoor LEDs and sunlight contain a broad range of visible wavelengths [38,47]. Accordingly, engineering the electronic structure and optical absorption range of sensing materials is an important strategy for developing practical visible-light-activated gas sensors.

Lee et al. employed size-controlled graphene quantum dots (GQDs) as bandgap-tunable photosensitizers for visible-light activation of In_2O_3 nanofiber-based NO_2 sensors (Fig. 4) [38]. The GQD-decorated sensors exhibited distinct size- and wavelength-dependent sensing characteristics under UV, blue, and green illumination (Fig. 4(a)). Under blue illumination, the GQD-decorated sensors showed selective responses toward NO_2 over the other tested gases, and the 7 nm GQD-decorated sensor exhibited the highest response of 97.1 toward 1 ppm NO_2 (Fig. 4(b)). The optical bandgap of the GQDs decreased from 3.3 to 1.9 eV as their size increased from 2 to 14 nm, owing to the enlarged sp^2 carbon core (Fig. 4(c)). This bandgap modulation altered the light-absorption characteristics of the In_2O_3/GQD sensing layers and shifted the effective photoactivation range from UV to visible light (Fig. 4(d)). Accordingly, the 2 nm GQD-decorated sensor showed its highest response under UV illumination, whereas the 4 and 7 nm GQD-decorated sensors showed maximum responses under blue illumination. The 7 nm GQD-decorated sensor also exhibited the highest resistance ratio between air and N_2 under blue illumination, indicating enhanced oxygen adsorption under this condition (Fig. 4(e)). In addition to bandgap engineering, GQDs provided chemical sensitization through oxygen-containing functional groups. DFT calculations showed that GQD functionalization increased the binding energies of NO_2 and O_2 on the In_2O_3 surface, particularly in the presence of C–OH and C–COOH groups (Fig. 4(f)). The size-dependent compositions of these functional groups further influenced the gas adsorption behavior of the sensing layer (Fig. 4(g)). Collectively, these findings demonstrate that GQDs simultaneously extend the photoactive wavelength range while enhancing NO_2 sensing through surface chemical sensitization.

In a related approach, Park et al. Bi-doped In_2O_3 nanofibers decorated with Au nanoparticles (NPs) for high-performance NO_2 sensing under visible-light illumination [47]. The sensing layer was fabricated by electrospinning In and Bi precursors,

followed by calcination and Au impregnation, forming mesoporous In_2O_3-based nanofibers with controlled Bi dopants and Au NPs. In this system, Bi dopants and Au NPs play complementary roles in photosensitization. Bi doping introduces mid-gap states in In_2O_3, extending optical absorption toward the visible-light region. This band-structure modulation enabled blue-light activation, and $Bi_xIn_{2-x}O_3$ (x = 0.04) exhibited the highest NO_2 response among the tested Bi contents. The optimized $Bi_xIn_{2-x}O_3$ sensor also showed a 46-fold higher response to NO_2 than pristine In_2O_3 under blue illumination, while maintaining low responses to interfering gases. Au NPs were further introduced as an additional photosensitizer to extend the photoactive wavelength range to green light. Under green illumination, Au-$Bi_xIn_{2-x}O_3$ (x = 0.04) showed a higher NO_2 response than $Bi_xIn_{2-x}O_3$ (x = 0.04), whereas the response under blue illumination decreased after Au decoration. This wavelength-dependent behavior indicates that Au NPs promote green-light activation through plasmonic hot-electron transfer to the Bi-doped In_2O_3 sensing layer. The sensing performance of this dual-photosensitizer system was evaluated under warm- and cool-white LED illumination. Au-$Bi_xIn_{2-x}O_3$ (x = 0.04) exhibited higher NO_2 responses under warm-white light with a strong green component, whereas $Bi_xIn_{2-x}O_3$ (x = 0.04) showed higher responses under cool-white light with a stronger blue component. Collectively, these findings demonstrate that dual-photosensitizer engineering provides an effective strategy for wavelength-selective photoactivation under diverse indoor lighting conditions, thereby expanding the practical applicability of light-activated gas sensors.

3. SYSTEM-LEVEL INTEGRATION FOR REAL-TIME MONITORING

Beyond materials engineering optimization, the practical deployment of light-activated gas sensors requires system-level integration for real-time monitoring. Such systems should provide stable light activation, low-power operation, reliable signal readout, and wireless data transmission. Recent studies have therefore combined photoactive sensing materials with ambient-light operation, μLED, wireless electronics, and mobile interfaces to enable gas monitoring beyond controlled laboratory environments [48-53].

3.1 Ambient-Light-Powered Wireless Gas Sensing Platforms for Plant Health Monitoring

Cho et al. integrated wafer-scale 3D TiO_2 nanostructures with wireless signal readout to demonstrate ambient-light-driven NO_2 monitoring in plant-associated environments (Fig. 5) [48]. This platform is relevant to plant health monitoring because NO_2 can induce oxidative stress in plants even at low concentrations, leading to reduced photosynthetic efficiency and impaired plant growth. By using ambient indoor light and sunlight as excitation sources, the platform does not require a dedicated integrated light source. The observed NO_2 responses under both UV and visible-light illumination indicate that the 3D TiO_2 sensor supports broadband photoactivation, thereby reducing the optical power required for continuous operation.

The highly ordered porous 3D TiO_2 structure was fabricated by sequential glancing angle deposition, enabling control over the total thickness, optical density, and gas-accessible pathways (Fig. 5(a)). As the number of deposition cycles increased, the structure showed enhanced light scattering and light diffusion over the UV and visible-light regions (Fig. 5(b)–(d)). The porous TiO_2 network also provided continuous diffusion pathways for NO_2 molecules. Among the tested structures, the 10-cycle 3D TiO_2 sensor showed the highest NO_2 response under UV illumination without thermal activation (Fig. 5(e)).

Stable operation under humid conditions is also required for plant-associated applications. The 3D TiO_2 sensor showed improved response and response–recovery characteristics over a wide relative humidity (RH) range under UV illumination, which was attributed to water-assisted surface reactions that promoted NO_2 adsorption at room temperature (Fig. 5(f)). In addition, the sensor showed concentration-dependent NO_2 responses under visible-light illumination through defect-assisted excitation, indicating that the sensing platform can operate beyond the intrinsic UV-active range of TiO_2 (Fig. 5(g)). The resulting sensing performance was comparable to that of previously reported light-activated gas sensors, supporting its potential for ambient-light-driven NO_2 detection (Fig. 5(h)).

To translate this material-level advantage into a practical monitoring system, the authors fabricated transparent 3D TiO_2 sensors on ITO interdigitated electrodes using a 4-inch wafer-scale process (Fig. 5(i)). The sensor was then integrated with a wireless microcontroller and mobile application, enabling real-time conversion of resistance changes into user-readable warning signals. Field demonstrations were conducted by placing the sensor near *Mentha suaveolens* under sunlight and indoor illumination (Fig. 5(j,k)). Collectively, these findings demonstrate a practical system-level strategy that integrates ambient-light operation, scalable fabrication, and wireless signal readout for real-time plant-health monitoring.

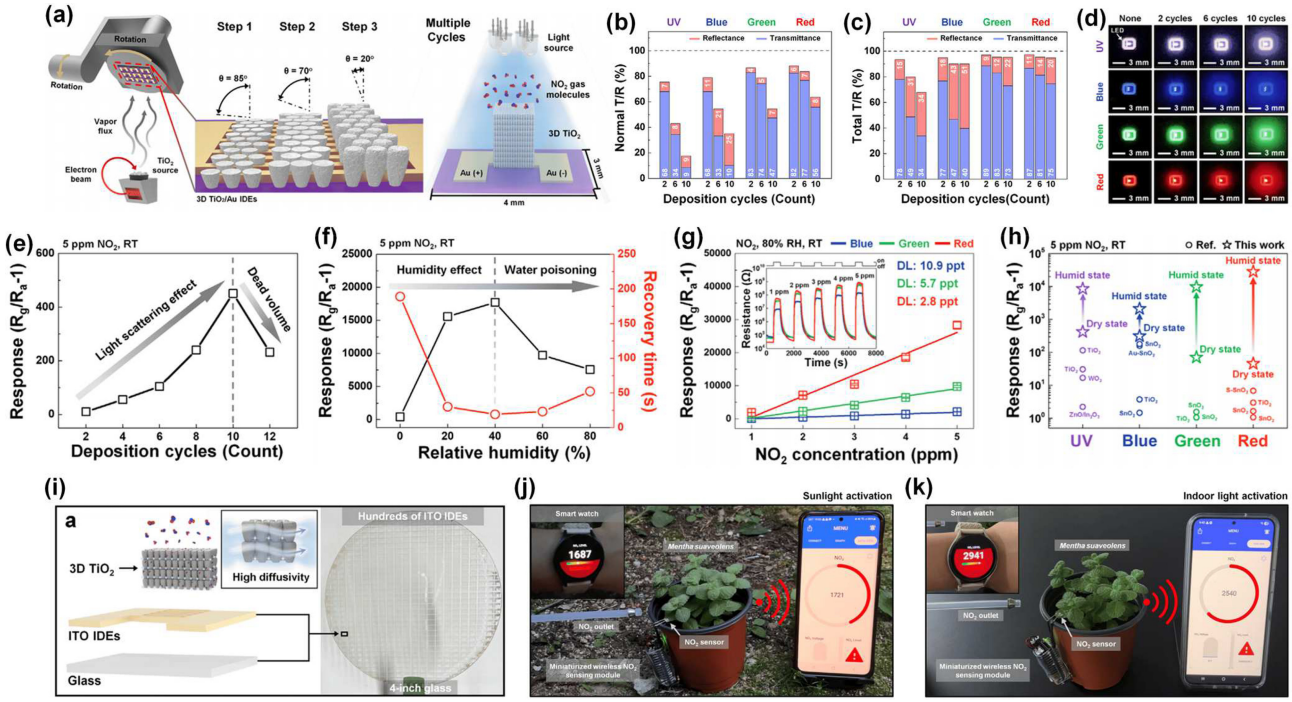

Fig. 5. Ambient-light-driven NO_2 sensing platform for real-time plant health monitoring. (a) Schematic illustration of the sequential glancing angle deposition process. (b,c) Normal and total transmittance/reflectance spectra of 3D TiO_2 nanostructures with different deposition cycles. (d) Photographs of light diffusion through 3D TiO_2 nanostructures under UV and visible-light illumination. (e) NO_2 responses of 3D TiO_2 sensors with different deposition cycles under UV illumination. (f) Humidity-dependent NO_2 response and recovery time of the optimized 3D TiO_2 sensor. (g) Concentration-dependent NO_2 responses under visible-light illumination in 80% RH. (h) Comparison of NO_2 sensing performance with previously reported light-activated gas sensors. (i) Schematic illustration and photograph of wafer-scale transparent 3D TiO_2/ITO sensor. (j,k) Real-time wireless NO_2 monitoring under sunlight and indoor illumination, respectively. Adapted from Ref. [48].

3.2 µLED-Integrated Gas Sensor Arrays for Low-Power Real-Time Detection

Unlike ambient-light-powered platforms, µLED-integrated systems provide stable and controllable photoactivation regardless of surrounding light conditions [54]. µLEDs are particularly attractive for this purpose because they provide localized illumination with minimal power consumption in a compact form factor [52,55]. In particular, directly integrating the sensing layer on or in close proximity to the µLED emission surface shortens the distance between the light source and sensing material, enabling efficient photoactivation with reduced optical loss.

Nam et al. developed a blue µLED-integrated gas sensor array based on SnO_2 NPs for low-power real-time tunable gas sensing (Fig. 6) [49]. SnO_2 NPs were directly loaded into the µLED cavity together with sensor electrodes and a passivation layer, forming a monolithic sensing platform (Fig. 6(a)). The integrated µLED emitted blue light with a peak wavelength of 453 nm, which matched the defect-assisted visible-light absorption of SnO_2 NPs (Fig. 6(b)–(d)). Despite the wide bandgap of SnO_2, defect states associated with oxygen vacancies and tin interstitials enabled efficient blue-light photoactivation. Therefore, the integrated blue µLED could activate the SnO_2 sensing layer at room temperature without external heating.

The NO_2 response strongly depended on the µLED power and showed a volcano-shaped trend, indicating that the photoactivation intensity should be optimized to balance light-driven surface reactions and gas accessibility within the sensing layer (Fig. 6(e,f)). At the optimized µLED power, the sensor showed a high response of 6928 to 5 ppm NO_2 with fast response and recovery times of 47 and 49 s, respectively. These results show that direct integration of the SnO_2 sensing layer with the blue µLED enables efficient photoactivation at microwatt-level power consumption of 63.2 µW.

To expand the detectable gas species, SnO_2 NPs were decorated with Au, Pd, and Pt. While the bare SnO_2 sensor showed the highest response to NO_2, the noble-metal-decorated sensors exhibited relatively high responses toward reducing gases under blue-light illumination (Fig. 6(g)). Au-

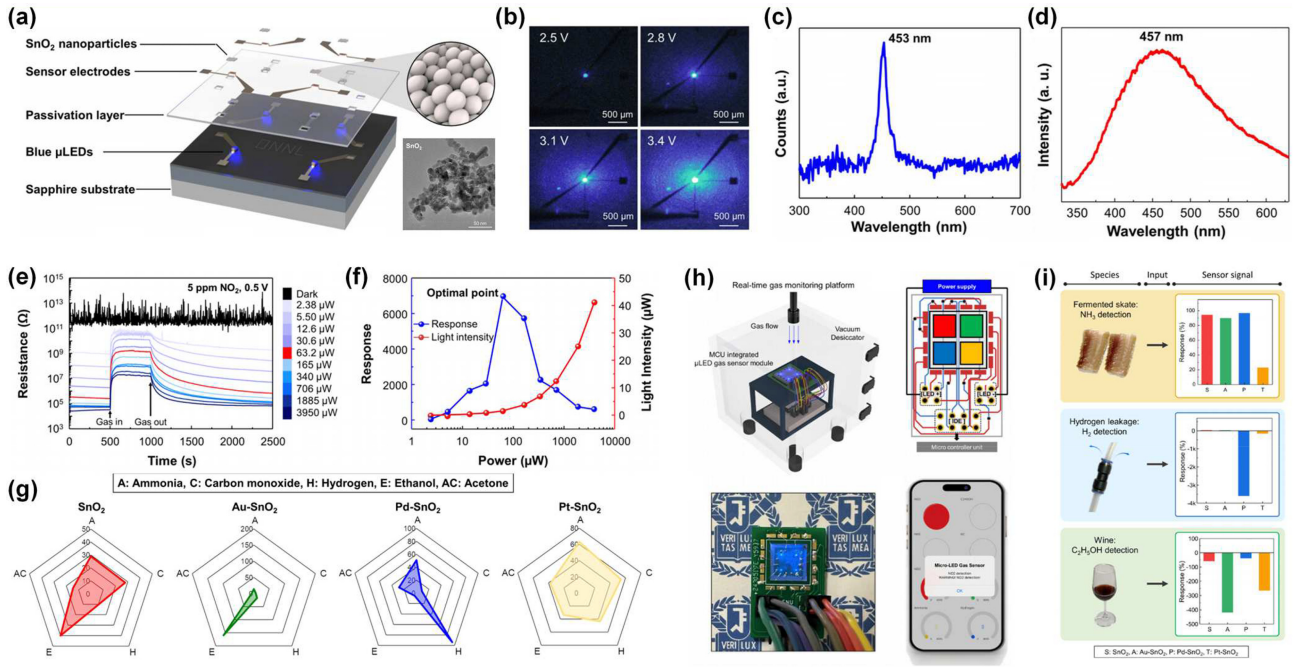

Fig. 6. Blue μLED-integrated gas sensor array for a low-power, real-time monitoring platform. (a) Schematic illustration of the μLED-integrated SnO_2 NPs-based gas sensor array. (b) Optical images of the μLED-integrated gas sensor array under different applied voltages. Photoluminescence spectra of (c) the blue μLED and (d) SnO_2 NPs. (e) Dynamic NO_2 sensing curves and (f) responses of SnO_2 NPs under different μLED powers. (g) Radar plots of SnO_2, Au-SnO_2, Pd-SnO_2, and Pt-SnO_2 sensors toward reducing gases under blue-light illumination. (h) Schematic illustrations and photographs of the real-time gas monitoring platform. (i) Practical demonstrations of the sensor array for detecting fermented skate, hydrogen leakage, and wine. Adapted from Ref. [49].

SnO_2 showed enhanced sensitivity to ethanol, Pd-SnO_2 exhibited a strong response to H_2, and Pt-SnO_2 showed broad responses to reducing gases, including NH_3. These response behaviors originate from noble-metal-dependent catalytic interactions with target gases, enabling tunable selectivity in the μLED-integrated sensor array.

The system-level applicability of this platform was further demonstrated by integrating the μLED sensor array with a microcontroller unit, customized printed circuit board, and mobile application (Fig. 6(h)). The integrated platform enabled simultaneous signal acquisition from multiple sensing channels and wireless communication for real-time gas monitoring. Practical demonstrations were conducted using fermented skate, hydrogen leakage, and wine as representative sources of NH_3, H_2, and ethanol, respectively (Fig. 6(i)). Each sample generated a different response pattern in the sensor array, showing the potential of the platform for electronic-nose applications. Overall, this study highlights that μLED-integrated gas sensor arrays provide an effective platform for low-power photoactivation, tunable gas selectivity, and real-time wireless monitoring in a compact system, offering a promising strategy for practical light-activated sensing platforms.

4. AI-ASSISTED ANALYSIS FOR SELECTIVE GAS RECOGNITION

Although materials engineering and system-level integration have improved the sensing performance and practical applicability of light-activated gas sensors, reliable gas recognition in realistic environments remains challenging. In practical environments, sensor signals are influenced by fluctuating light intensity, spectral variations, multiple gas species, humidity, temperature fluctuations, and long-term signal drift. These factors can alter the photoactivation process and generate overlapping responses between target and interfering gases. AI-assisted analysis can extract useful features from these complex sensing signals to improve gas classification and concentration estimation [22]. This section highlights data-driven strategies that use dynamic light modulation and sensor-response analysis for selective gas recognition.

4.1 Time-Varying Light Modulation for AI-Assisted Gas Identification

Conventional light-activated gas sensors typically operate under constant illumination, where the light source provides a fixed photoactivation input to the sensing material.

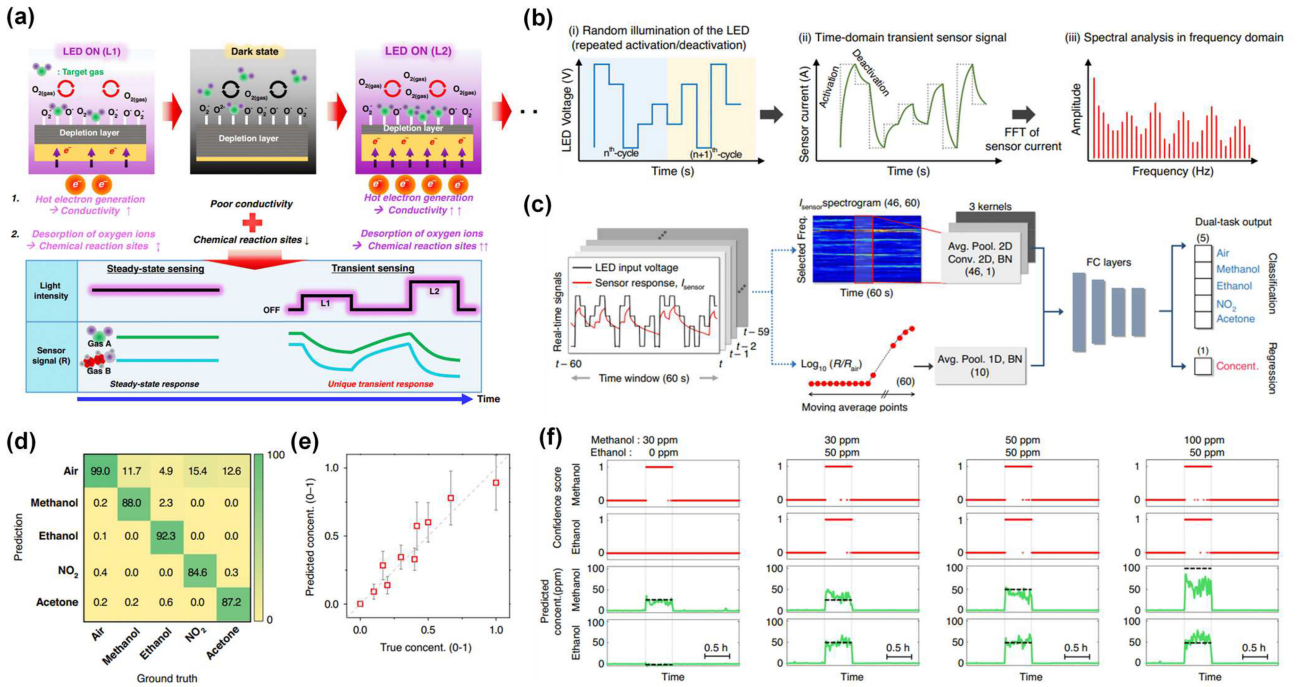

Fig. 7. Dynamic light modulation for AI-assisted gas identification. (a) Schematic illustration of time-variant photoactivation and deactivation for generating gas-specific transient responses. (b) Pseudorandom μLED illumination and spectral transformation of the transient sensor signal. (c) D-CNN architecture for simultaneous gas classification and concentration regression using the transient spectrogram and moving-average response. (d,e) Classification and quantification performance for air, methanol, ethanol, NO_2, and acetone. (f) Real-time identification of binary methanol/ethanol mixtures. Adapted from Ref. [56].

Consequently, the sensor response often converges to a steady state, making it difficult to distinguish gases with similar response characteristics. This limitation hinders selective gas identification when only a single sensing channel is used. Although sensor arrays can provide multidimensional response patterns, they also increase device complexity, power consumption, and system volume. Therefore, generating richer sensing information from a single light-activated sensor is important for compact and low-power gas sensing platforms [56].

Time-varying light modulation addresses this issue by dynamically changing the light intensity during gas exposure (Fig. 7). The repeated change in photoactivation alters the carrier population and surface reaction state of the sensing material, thereby generating transient response patterns rather than a simple steady-state signal. Because the adsorption, desorption, and surface reaction kinetics differ depending on the gas species, these transient responses can contain gas-specific information. In this approach, the light source serves not only as an activation component but also as an external modulation input for extracting dynamic sensing features.

Cho et al. demonstrated this concept using a single μLED-embedded photoactivated gas sensor combined with deep-learning-based analysis (Fig. 7(a)). The sensor consisted of a nanoporous Au NP-decorated In_2O_3 sensing layer integrated with a μLED for rapid and localized photoactivation. A pseudorandom voltage input was applied to the μLED rather than constant illumination, generating forced transient sensor responses. The time-domain current signal was converted into frequency-domain spectra and represented as spectrogram data (Fig. 7(b)). These spectral features reflect both the response magnitude and the dynamic characteristics induced by time-varying illumination.

The extracted transient spectrogram and moving-average response were then analyzed using a deep convolutional neural network (D-CNN) designed for simultaneous gas classification and concentration regression (Fig. 7(c)). The D-CNN successfully distinguished air, methanol, ethanol, NO_2, and acetone using the transient features generated from a single sensing channel (Fig. 7(d)). In addition, the regression output provided concentration estimation, showing that the time-modulated signal contains quantitative information as well as gas-specific classification features (Fig. 7(e)). The same framework was further extended to binary methanol/ethanol mixture analysis by using confidence scores and predicted concentrations for each gas component (Fig. 7(f)). Overall, this study highlights that temporal control of photoactivation can provide the analytical capability of a single sensing channel when combined with AI-based signal analysis.

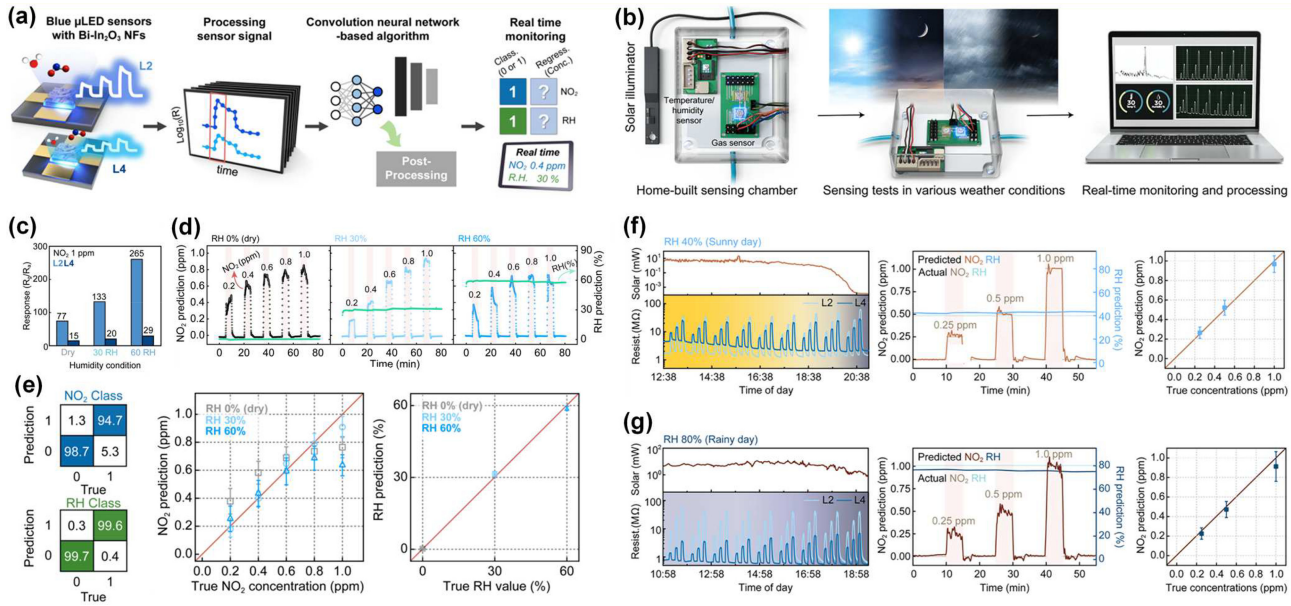

Fig. 8. Weather-independent gas detection through deep learning. (a) Schematic illustration of CNN-based analysis using blue μLED-integrated Bi–In_2O_3 nanofiber sensors operated under two light-intensity conditions for simultaneous NO_2 and RH prediction. (b) Outdoor sensing setup for real-time monitoring under different weather conditions. (c) Humidity-dependent NO_2 responses of the Bi–In_2O_3 sensor. (d) Real-time prediction of NO_2 concentration and RH under dry, 30% RH, and 60% RH conditions. (e) Classification and regression performance for NO_2 and RH prediction. (f,g) Outdoor NO_2 and RH prediction results under sunny and rainy conditions, respectively. Adapted from Ref. [57].

4.2 Weather-Independent Gas Detection through Deep Learning Analysis

To overcome humidity variations under real-world weather conditions, Lee et al. developed a blue μLED-integrated Bi-doped In_2O_3 nanofiber platform combined with convolutional neural network (CNN)-based analysis for robust gas detection (Fig. 8) [57]. The platform employed two Bi–In_2O_3 sensing channels operated under lower- and higher-intensity blue μLED conditions (denoted as L2 and L4, respectively). The resistance signals from the two channels were processed using a CNN for simultaneous prediction of NO_2 concentration and RH level (Fig. 8(a)). For outdoor validation, the μLED-integrated sensing system was installed in a custom-built chamber equipped with humidity, temperature, and optical-power monitoring modules. The sensing signals were collected and processed in real time while the system was tested under different weather conditions (Fig. 8(b)). This configuration enabled reliable NO_2 detection under realistic outdoor environments with varying humidity and illumination conditions, demonstrating the robustness of the AI-assisted sensing platform.

The two light-intensity conditions showed different NO_2 sensing behaviors. Under exposure to 1 ppm NO_2, the lower-intensity L2 condition (58 μW) showed a higher response of 77.7 with a response time of 29 s, whereas the higher-intensity L4 condition (485 μW) showed a lower response of 11.2 with a faster response time of 22 s (Fig. 8(c)). The NO_2 responses of both channels increased with increasing RH, indicating a water-promotion effect in the Bi–In_2O_3 sensing reaction. Under L2 illumination, the response increased from 77 under dry conditions to 133 at 30% RH and 265 at 60% RH. Under L4 illumination, the response increased from 15 to 20 and 29 over the same RH range. These different response magnitudes and response kinetics provided complementary sensing profiles for NO_2 and RH analysis. The CNN model was trained using gas sensing dataset obtained at NO_2 concentrations of 0.2–1.0 ppm under dry, 30% RH, and 60% RH conditions. The model enabled real-time prediction of NO_2 concentration and RH level under each humidity condition (Fig. 8(d)). The classification and regression results further confirmed the reliable separation of NO_2- and RH-related response features (Fig. 8(e)). The classification accuracies were 97.5% for NO_2 and 99.6% for RH, while the mean absolute errors for concentration prediction were 24% for NO_2 and 6.2% for RH.

To demonstrate the practical adaptability of the proposed platform, outdoor sensing performance was evaluated under both sunny and rainy conditions. The system was tested over nine NO_2 exposure cycles from 0.25 to 1.0 ppm under approximately 40% RH on a sunny day and 80% RH on a rainy day. Although the solar power and resistance profiles differed between the two weather conditions, the CNN-assisted

Table 1. Summary of representative light-activated gas sensors discussed in this review.

Sensing materials	Light source	Target gas	Conc. (ppm)	Response	LOD (ppt)	RH (%)	AI Model (Accuracy)	Power consumption (μW)	Ref.
3D TiO_2	UV LED (365 nm)	NO_2	5	30.6 122.2	202.4 –	Dry 50	–	800	[40]
3D ZnO/ZIF-8	UV LED (365 nm)	NO_2	0.1	1.2	375	Dry	–	–	[42]
5MMM/TiO_2	UV LED (365 nm)	HCHO	2.5	714.9 695.2	3800 –	Dry 20	–	–	[43]
In_2O_3/GQD-7	Blue LED (460 nm)	NO_2	0.2	6.9 8.8	–	Dry 75	–	–	[38]
$Bi_{0.04}In_{1.96}O_3$	Cool-white LED	NO_2	0.8	75.7	–	Dry	–	–	[47]
Au–$Bi_{0.04}In_{1.96}O_3$	Warm-white LED	NO_2	0.4	33.3 56	–	Dry 50	–	–	[47]
3D TiO_2	UV LED (365 nm)	NO_2	5	451 8521	45.2 0.0663	Dry 80	– –	– –	[48]
SnO_2 NPs	Blue-μLED (453 nm)	NO_2	5 2	6928 ~10^3	4.5	Dry 80	–	63.2	[49]
Au-SnO_2 NPs		C_2H_5OH	100	~1.3	–			2028	
Pd-SnO_2 NPs		H_2	500	~230		Dry		2.4	
Pt-SnO_2 NPs		NH_3	100	~0.3				73.4	
Au NPs@In_2O_3	UV-μLED (395 nm)	CH_3OH C_2H_5OH CH_3COCH_3 NO_2	100 100 1000 20	~0.8 ~0.6 ~0.4 ~2.7	–	Dry	D-CNN (96.99%)	526	[56]
3Bi-In_2O_3 NFs	Blue-μLED (455 nm, L2)	NO_2	1	77.7 264.9	–	Dry 60	CNN, (97.5%, NO_2) (99.6%, RH)	58	[57]
	Blue-μLED (455 nm, L4)			11.2 29		Dry 60		485	

system predicted NO_2 concentration and RH in real time under both conditions (Fig. 8(f,g)). This platform showed 98% NO_2 identification accuracy, with average prediction errors of 11.8% for NO_2 concentration and 10.4% for RH. These results demonstrate that CNN-based analysis can distinguish NO_2-related response changes from humidity-dependent variations, supporting reliable gas detection under variable outdoor conditions.

5. CONCLUSIONS

In this review, recent advances in light-activated gas sensors have been discussed from the perspectives of materials engineering, system-level integration, and AI-assisted analysis. Light activation enables room-temperature gas sensing through photogenerated charge carriers and light-driven surface reactions, providing an alternative to conventional thermal activation. Recent studies have further expanded photoactivation from UV toward visible-light operation through the design of sensing materials and light sources. Materials engineering can improve light utilization, gas accessibility, selectivity, and visible-light responsiveness, while functional overlayers regulate molecular transport and suppress interfering gases. Dopants, GQDs, heterointerfaces, and plasmonic photosensitizers can further extend the optical response of wide-bandgap metal oxides. Collectively, these advances indicate that high sensing performance requires a balance among light absorption, charge-carrier separation, gas transport, and surface reactions. System-level integration and AI-assisted analysis are also important for practical

applications. Ambient-light-driven and μLED-integrated platforms enable low-power and controllable photoactivation, while wireless electronics and mobile interfaces support real-time monitoring. In addition, time-varying light modulation and data-driven analysis can improve gas recognition and compensate for environmental variations. Table 1 summarizes the sensing materials, light sources, target gases, gas responses, theoretical limit of detection (LOD), humidity conditions, power consumption, and AI-assisted analysis of representative light-activated gas sensors discussed in this review. Future studies should focus on the co-design of sensing materials, light sources, device structures, and analytical methods. Reliable evaluation under mixed gases, varying humidity and temperature, changing light conditions, and long-term operation will be essential for practical deployment. Collectively, these efforts will advance light-activated gas sensors toward reliable, low-power platforms for environmental, wearable, and mobile sensing applications.

CRediT Authorship Contribution

Yun-Haeng Cho: Conceptualization, Investigation, Writing – original draft, Writing – review, and editing, Visualization. **Jun Min Suh:** Funding acquisition, Supervision, Project administration, Writing – review and editing.

Declaration of Competing Interest

The authors declare that they have no known competing financial interests or personal relationships that could have appeared to influence the work reported in this paper.

Acknowledgements

This work was supported by the National Research Foundation of Korea (NRF) grant funded by the Korea Government (MSIT) (RS-2025-24803330) and the New Faculty Startup Fund from Seoul National University. The Inter-University Semiconductor Research Center, Institute of Engineering Research, and Soft Foundry Institute at Seoul National University provided research facilities for this work.

REFERENCES

[1] J.H. Chung, D.Y. An, W.-S. Choi, Y.-H. Cho, E.J. Ko, J.Y. An, et al., Dual sulfur-specific pathways in Ag-sensitized Cr_2O_3 nanoarchitectures for robust H_2S discrimination in complex gas mixtures, Chem. Eng. J. 542 (2026) 177723.

[2] J.H. Chung, Y.-H. Cho, J. Hwang, S. Lee, S. Lee, S.-H. Park, et al., Heterostructures of SnO_2-decorated Cr_2O_3 nanorods for highly sensitive H_2S detection, J. Sens. Sci. Technol. 33 (2024) 40–47.

[3] J. Hwang, J.H. Chung, H.J. Kim, S.-H. Park, Y.-H. Cho, S. Sohn, et al., CeO_2/NiO heterostructures for extremly-selective acetone detection: The critical role of the Ce^{3+}/Ce^{4+} ratio in NiO nanodomes, Sens. Actuators B Chem. 442 (2025) 138070.

[4] J.H. Chung, D.-S. Kim, S.-K. Bae, Y.-H. Cho, H. Yun, M.-C. Kim, et al., Dual engineering of helical SnO_2 nanostructures and Co^{2+}/Co^{3+} valence state for ultra-selective acetone detection, Chem. Eng. J. 532 (2026) 174591.

[5] J. Hwang, S.-H. Park, Y.-S. Shim, S. Sohn, J.H. Chung, Y.-H. Cho, et al., Fast and selective isoprene gas sensor: Influence of polystyrene size and role of the Au catalyst on gas sensing properties, Sens. Actuators B Chem. 422 (2025) 136500.

[6] J.P.P. Rajakumar, J.-H. Choi, Helmet-mounted real-time toxic gas monitoring and prevention system for workers in confined places, Sensors 23 (2023) 1590.

[7] P. Schneider, N. Castell, M. Vogt, F.R. Dauge, W.A. Lahoz, A. Bartonova, Mapping urban air quality in near real-time using observations from low-cost sensors and model information, Environ. Int. 106 (2017) 234–247.

[8] L.-Y. Chang, M.-Y. Chuang, H.-W. Zan, H.-F. Meng, C.-J. Lu, P.-H. Yeh, et al., One-minute fish freshness evaluation by testing the volatile amine gas with an ultrasensitive porous-electrode-capped organic gas sensor system, ACS Sens. 2 (2017) 531–539.

[9] J. Burgués, M.D. Esclapez, S. Doñate, S. Marco, RHINOS: A lightweight portable electronic nose for real-time odor quantification in wastewater treatment plants, iScience 24 (2021) 103371.

[10] W. Heng, S. Yin, J. Min, C. Wang, H. Han, E. Shirzaei Sani, et al., A smart mask for exhaled breath condensate harvesting and analysis, Science 385 (2024) 954–961.

[11] A.H. Assen, O. Yassine, O. Shekhah, M. Eddaoudi, K.N. Salama, MOFs for the sensitive detection of ammonia: Deployment of fcu-MOF thin films as effective chemical capacitive sensors, ACS Sens. 2 (2017) 1294–1301.

[12] J. Dai, Y. Li, H. Ruan, Z. Ye, N. Chai, X. Wang, et al., Fiber optical hydrogen sensor based on WO_3–Pd_2Pt–Pt nanocomposite films, Nanomaterials 11 (2021) 128.

[13] H.P. Lang, R. Berger, F. Battiston, J.-P. Ramseyer, E. Meyer, C. Andreoli, et al., A chemical sensor based on a micromechanical cantilever array for the identification of gases and vapors, Appl. Phys. A 66 (1998) S61–S64.

[14] J. Wang, Y. Liu, H. Zhou, Y. Wang, M. Wu, G. Huang, et al., Thermal conductivity gas sensor with enhanced flow-rate independence, Sensors 22 (2022) 1308.

[15] Q. Hu, P. Solomon, L. Österlund, Z. Zhang, Nanotransistor-based gas sensing with record-high sensitivity enabled by electron trapping effect in nanoparticles, Nat. Commun. 15 (2024) 5259.

[16] H. Hong, J. Sun, C. Wu, Z. Liu, High performance mixed potential type NO_2 gas sensor based on porous YSZ layer formed with graphite doping, Sensors 19 (2019) 3337.

[17] Y. Kim, J.M. Suh, J. Shin, Y. Liu, H. Yeon, K. Qiao, et al., Chip-less wireless electronic skins by remote epitaxial freestanding compound semiconductors, Science 377 (2022) 859–864.

[18] A. Sharma, S.B. Eadi, H. Noothalapati, M. Otyepka, H.-D.

Lee, K. Jayaramulu, Porous materials as effective chemiresistive gas sensors, Chem. Soc. Rev. 53 (2024) 2530–2577.
[19] P. Yu, L. Wang, H. Liu, A. Yu, X. Liu, Z. Yang, Room-temperature H_2 gasochromic behaviors of highly sensitive hexagonal phase WO_3/Pt nanorods for eye-readable hydrogen leakage detection, Sens. Actuators B Chem. 427 (2025) 137221.
[20] M.V. Nikolić, V. Milovanović, Z.Z. Vasiljević, Z. Stamenković, Semiconductor gas sensors: Materials, technology, design, and application, Sensors 20 (2020) 6694.
[21] J.H. Chung, H.-G. Kim, Y.-H. Cho, J. Hwang, S.-H. Park, S.W. Sohn, et al., Highly ordered In_2O_3 zig-zag nanocolumns for selective detection of acetone, J. Surf. Sci. Eng. 57 (2024) 38–48.
[22] Y.-H. Cho, D.-S. Kim, J.H. Seo, J.H. Chung, Z. Park, K.C. Kwon, et al., Artificial olfactory system enabled by ultralow chemical sensing variations of 1D SnO_2 nanoarchitectures, Adv. Sci. 12 (2025) 2501293.
[23] S.-H. Sung, J.M. Suh, Y.J. Hwang, H.W. Jang, J.G. Park, S.C. Jun, Data-centric artificial olfactory system based on the eigengraph, Nat. Commun. 15 (2024) 1211.
[24] J. Burgués, S. Marco, Low power operation of temperature-modulated metal oxide semiconductor gas sensors, Sensors 18 (2018) 339.
[25] S.M. Majhi, A. Mirzaei, H.W. Kim, S.S. Kim, T.W. Kim, Recent advances in energy-saving chemiresistive gas sensors: A review, Nano Energy 79 (2021) 105369.
[26] T. Pham, G. Li, E. Bekyarova, M.E. Itkis, A. Mulchandani, MoS_2-based optoelectronic gas sensor with sub-parts-per-billion limit of NO_2 gas detection, ACS Nano 13 (2019) 3196–3205.
[27] H. Tabata, H. Matsuyama, T. Goto, O. Kubo, M. Katayama, Visible-light-activated response originating from carrier-mobility modulation of NO_2 gas sensors based on MoS_2 monolayers, ACS Nano 15 (2021) 2542–2553.
[28] S. Park, S. An, Y. Mun, C. Lee, UV-enhanced NO_2 gas sensing properties of SnO_2-core/ZnO-shell nanowires at room temperature, ACS Appl. Mater. Interfaces 5 (2013) 4285–4292.
[29] J. Gong, Y. Li, X. Chai, Z. Hu, Y. Deng, UV-light-activated ZnO fibers for organic gas sensing at room temperature, J. Phys. Chem. C 114 (2010) 1293–1298.
[30] R. Kumar, N. Goel, M. Kumar, UV-activated MoS_2 based fast and reversible NO_2 sensor at room temperature, ACS Sens. 2 (2017) 1744–1752.
[31] K. Lee, Y.-M. Jo, M.S. Sohn, M. Jeon, C. Kim, O. Gul, et al., Photoactivated conductive MOF thin film arrays on micro-LEDs for chemiresistive gas sensing, Nat. Commun. 16 (2025) 9612.
[32] Z.Q. Zheng, J. Yao, B. Wang, G. Yang, Light-controlling, flexible and transparent ethanol gas sensor based on ZnO nanoparticles for wearable devices, Sci. Rep. 5 (2015) 11070.
[33] M. Šetka, M. Claros, O. Chmela, S. Vallejos, Photoactivated materials and sensors for NO_2 monitoring, J. Mater. Chem. C 9 (2022) 16804–16827.
[34] H. Wang, J. Bai, M. Dai, K. Liu, Y. Liu, L. Zhou, et al., Visible light activated excellent NO_2 sensing based on 2D/2D ZnO/g-C_3N_4 heterojunction composites, Sens. Actuators B Chem. 304 (2020) 127287.
[35] A. Turlybekuly, Y. Shynybekov, B. Soltabayev, G. Yergaliuly, A. Mentbayeva, The cross-sensitivity of chemiresistive gas sensors: Nature, methods, and peculiarities: A systematic review, ACS Sens. 9 (2024) 6358–6371.
[36] S. Park, S.H. Jeon, H. Kim, J. Philips, D.H. Oh, J. Ahn, et al., Imparting metal oxides with high sensitivity toward light-activated NO_2 detection via tailored interfacial chemistry, Adv. Funct. Mater. 33 (2023) 2214008.
[37] T.H. Eom, S.H. Cho, J.M. Suh, T. Kim, J.W. Yang, T.H. Lee, et al., Visible light driven ultrasensitive and selective NO_2 detection in tin oxide nanoparticles with sulfur doping assisted by L-cysteine, Small 18 (2022) 2106613.
[38] J. Lee, M. Kim, S. Park, J. Lee, Q. Chen, J. Kim, et al., Bandgap-engineered graphene quantum dot photosensitizers for tunable light spectrum-activated NO_2 sensors, ACS Nano 19 (2025) 32732–32743.
[39] Y.-M. Jo, K. Lim, J.W. Yoon, Y.K. Jo, Y.K. Moon, H.W. Jang, et al., Visible-light-activated type II heterojunction in Cu_3(hexahydroxytriphenylene)$_2$/Fe_2O_3 hybrids for reversible NO_2 sensing: Critical role of π–π^* transition, ACS Cent. Sci. 7 (2021) 1176–1182.
[40] D. Cho, J.M. Suh, S.-H. Nam, S.Y. Park, M. Park, T.H. Lee, et al., Optically activated 3D thin-shell TiO_2 for super-sensitive chemoresistive responses: Toward visible light activation, Adv. Sci. 8 (2020) 2001883.
[41] P.M. Bulemo, D.-H. Kim, H. Shin, H.J. Cho, W.T. Koo, S.J. Choi, et al., Selectivity in chemiresistive gas sensors: Strategies and challenges, Chem. Rev. 125 (2025) 4111–4183.
[42] J. Lee, H. Lee, T.H. Bae, D. Cho, M. Choi, G. Bae, et al., 3D ZnO/ZIF-8 hierarchical nanostructure for sensitive and selective NO_2 sensing at room temperature, Small Struct. 5 (2024) 2300503.
[43] Y.K. Jo, S.-Y. Jeong, Y.K. Moon, Y.-M. Jo, J.-W. Yoon, J.-H. Lee, Exclusive and ultrasensitive detection of formaldehyde at room temperature using a flexible and monolithic chemiresistive sensor, Nat. Commun. 12 (2021) 4955.
[44] J. Lee, M. Kim, S. Park, J. Ahn, I.-D. Kim, Materials engineering for light-activated gas sensors: Insights, advances, and future perspectives, Adv. Mater. 37 (2025) e08204.
[45] F. Xu, H.-P. Ho, Light-activated metal oxide gas sensors: A review, Micromachines 8 (2017) 333.
[46] A.S. Chizhov, M.N. Rumyantseva, R.B. Vasiliev, D.G. Filatova, K.A. Drozdov, I.V. Krylov, et al., Visible light activation of room temperature NO_2 gas sensors based on ZnO, SnO_2 and In_2O_3 sensitized with CdSe quantum dots, Thin Solid Films 618 (2016) 253–262.
[47] S. Park, M. Kim, Y. Lim, D.H. Oh, J. Ahn, C. Park, et al., Dual-photosensitizer synergy empowers ambient light photoactivation of indium oxide for high-performance NO_2 sensing, Adv. Mater. 36 (2024) 2313731.

[48] Y.-H. Cho, K. Hong, J.H. Seo, J.H. Chung, J. Lee, S.-H. Nam, et al., Scalable photoactive NO_2-sensing framework for plant health monitoring, Adv. Sci. 13 (2026) e18368.
[49] G.B. Nam, J.-E. Ryu, T.H. Eom, S.J. Kim, J.M. Suh, S. Lee, et al., Real-time tunable gas sensing platform based on SnO_2 nanoparticles activated by blue micro-light-emitting diodes, Nano-Micro Lett. 16 (2024) 261.
[50] R.S. Ghuge, S.M. Rekha, H.K. Vikraman, S.V. Jayaraman, M.S.R.N. Kiran, S.V. Bhat, et al., Transparent TiO_2/MoO_3 heterojunction-based photovoltaic self-powered triethylamine gas sensor with IoT-enabled smartphone interface, ACS Sens. 9 (2024) 6592–6604.
[51] S.M. Rekha, R.S. Ghuge, H.K. Vikraman, M.S.R.N. Kiran, Y. Sivalingam, S.V. Bhat, ZnO/CuI heterojunction UV-photovoltaic gas sensor for self-powered IoT-integrated n-butylamine VOC detection, Adv. Mater. Technol. 10 (2025) 70049.
[52] I. Cho, Y.C. Sim, M. Cho, Y.-H. Cho, I. Park, Monolithic micro light-emitting diode/metal oxide nanowire gas sensor with microwatt-level power consumption, ACS Sens. 5 (2020) 563–570.
[53] I. Cho, Y.C. Sim, K. Lee, M. Cho, J. Park, M. Kang, et al., Nanowatt-level photoactivated gas sensor based on fully-integrated visible microLED and plasmonic nanomaterials, Small 19 (2023) 2207165.
[54] N. Markiewicz, O. Casals, C. Fabrega, I. Gràcia, C. Cané, H.S. Wasisto, et al., Micro light plates for low-power photoactivated gas sensors, Appl. Phys. Lett. 114 (2019) 053508.
[55] O. Casals, N. Markiewicz, C. Fabrega, I. Gràcia, C. Cané, H.S. Wasisto, et al., A parts per billion sensor for NO_2 with microwatt power requirements based on micro light plates, ACS Sens. 4 (2019) 822–826.
[56] I. Cho, K. Lee, Y.C. Sim, J.-S. Jeong, M. Cho, H. Jung, et al., Deep-learning-based gas identification by time-variant illumination of a single micro-LED-embedded gas sensor, Light Sci. Appl. 12 (2023) 95.
[57] K. Lee, M. Kim, Y. Kwon, S. Park, Y. Lim, D. Kwak, et al., Enabling weather-independent gas detection through deep learning on light-activated sensors, ACS Nano 19 (2025) 38327–38339.

Yun-Haeng Cho is a Ph.D. student in the Department of Materials Science and Engineering at Seoul National University, where he is supervised by Prof. Jun Min Suh. He received his B.S. and M.S. degrees through an integrated B.S.–M.S. program in the School of Energy, Materials and Chemical Engineering at Korea University of Technology and Education (KOREATECH), where he conducted research under the supervision of Prof. Young-Seok Shim. His research interests include micro/nanostructured materials for chemiresistive gas sensors and gasochromic membranes.

Jun Min Suh is an Assistant Professor in the School of Transdisciplinary Innovations and the Department of Materials Science and Engineering at Seoul National University. He received his B.S. and Ph.D. degrees in Materials Science and Engineering from Seoul National University and was a postdoctoral associate in the Department of Mechanical Engineering at the Massachusetts Institute of Technology (MIT). His research interests include freestanding single-crystalline membranes, monolithic 3D integration, intelligent semiconductors, multifunctional sensors, and heterogeneous material integration for next-generation computing, communication, and healthcare systems.